Growth of fullerene-like carbon nitride thin solid films by reactive magnetron sputtering; role of low-energy ion irradiation in determining microstructure and mechanical properties

J. Neidhardt,[a] Zs. Czigány,[b] I. F. Brunell,[c] and L. Hultman
Thin Film Division, Department of Physics, IFM, Linköping University, S-58183 Linköping, Sweden

(Received 16 September 2002; accepted 22 November 2002)

Fullerene-like (FL) carbon nitride (CN_x) films were deposited on Si (100) substrates by dc reactive, unbalanced, magnetron sputtering in a N_2/Ar mixture from a high-purity pyrolythic graphite cathode in a dual-magnetron system with coupled magnetic fields. The N_2 fraction in the discharge gas (0%–100%) and substrate bias (−25 V; −40 V) was varied, while the total pressure (0.4 Pa) and substrate temperature (450 °C) was kept constant. The coupled configuration of the magnetrons resulted in a reduced ion flux density, leading to a much lower average energy per incorporated particle, due to a less focused plasma as compared to a single magnetron. This enabled the evolution of a pronounced FL microstructure. The nitrogen concentration in the films saturated rapidly at 14–18 at. %, as determined by elastic recoil analysis, with a minor dependence on the discharge conditions. No correlations were detected between the photoelectron N1*s* core level spectra and the different microstructures, as observed by high-resolution electron microscopy. A variety of distinct FL structures were obtained, ranging from structures with elongated and aligned nitrogen-containing graphitic sheets to disordered structures, however, not exclusively linked to the total N concentration in the films. The microstructure evolution has rather to be seen as in equilibrium between the two competing processes of adsorption and desorption of nitrogen-containing species at the substrate. This balance is shifted by the energy and number of arriving species as well as by the substrate temperature. The most exceptional structure, for lower N_2 fractions, consists of well-aligned, multi-layered circular features (nano-onions) with an inner diameter of approximately 0.7 nm and successive shells at a distance of ~0.35 nm up to a diameter of 5 nm. It is shown that the intrinsic stress formation is closely linked with the evolution and accommodation of the heavily bent fullerene-like sheets. The FL CN_x structures define the mechanical response of the films as revealed by nano-indentation. The material is highly elastic and fracture tough, and has reasonable hardness and elastic modulus values. On a nano-structured level, it is inferred the CN_x stores deformation energy elastically by compression of the interplanar lattice spacing and buckling of the sheets, while crosslinks between sheets prevent gliding. Increasing the bias voltage from −25 to −40 V multiplies hardness and modulus values, while keeping their high ratio of up to 0.2, due to a higher degree of cross-linking. © *2003 American Institute of Physics.* [DOI: 10.1063/1.1538316]

INTRODUCTION

Fullerene-like (FL) carbon nitride (CN_x) denotes a range of promising CN_x compounds that exhibits outstanding properties originating from a unique microstructure. The structure consists of bent and intersecting nitrogen-containing graphitic basal planes. The orientation, radius of curvature, and the degree of cross-linking between them determine the structure and the properties of the FL material. Such material deforms elastically over a wide range due to a bending and buckling of the atomic sheets and a lack of slip systems. The comparatively low elastic modulus (<130 GPa), together with a reasonable high hardness, results in a fracture-tough material. These properties, combined with the fairly low coefficient of friction, yield in an interesting candidate for tribological coatings.[1–3]

The most well-developed FL microstructures in CN_x have been observed for magnetron sputtered films. One of the limiting factors, which suppresses this kind of structure evolution in many other thin film deposition processes is, in our opinion, exposure to high-flux and high-energy ion bombardment. Such methods, for example, arc evaporation, ion-beam-assisted deposition, laser ablation, and to a certain extent rf sputtering, usually employ an ion-to-neutral arrival rate ratio in excess of 10. This high average energy per incorporated particle leads on the one hand to an elevated apparent nitrogen content, but on the other hand hinders the growth of any ordered structure. The resulting material is thus mostly amorphous. No convincing evidence is reported in the literature for the synthesis of crystalline carbon nitride by these methods. Growth of CN_x films with some structural order, however, is possible by laser ablation[4] and reactive dc magnetron sputtering[5] due to a reduced energy level, by

[a]Electronic mail: jorne@ifm.liu.se
[b]Also with: Research Institute for Technical Physics and Materials Science, P.O. Box 49, Budapest H-1525, Hungary.
[c]Present address: Department of Chemical Engineering, Carnegie Mellon University, Pittsburgh, PA 15210.

Downloaded 17 Mar 2003 to 148.6.104.15. Redistribution subject to AIP license or copyright, see http://ojps.aip.org/japo/japcr.jsp

means of a reduced bias or increased target–substrate distance.

During sputtering, only a low fraction of the flux is ionized, and the arriving particles are mainly neutrals, with thermal energies.[6] These "gentler" growth conditions might be the requirement for the evolution of the so-called "fullerene-like" CN_x structure. The key for understanding the structure formation is nitrogen incorporation. It plays a major role during growth, since it gives upon incorporation the surrounding carbon matrix a radical nature, which might provide for cross-linking at C sites.[7–9] Another possibility for cross-linking might be bond rotation around an sp^2 C–C bond, resulting in a three-dimensional structure. The planar configuration of a carbon sp^2 network is due to the fixed bond angles by the overlap of the π-orbital perpendicular to the σ-bond. The incorporation of N, which brings an extra electron and a higher electronegativity, might also cause the disruption of the π-electron cloud, giving rise to nonplanar C–C bonds. For the formation of FL structures, the substitution of N for C is also important, since it reduces the energy barrier to form pentagons,[5] thus inducing the curvature inherent to the fullerenes.

Previous work has shown that the properties of FL CN_x films grown by dc unbalanced reactive magnetron sputtering can be varied over a wide range, spanning from under-dense, soft, amorphous structures to hard, elastic, FL materials.[5,10] This is realized by tuning the growth conditions, such as substrate temperature, bias voltage, target power, total pressure, and nitrogen partial pressure. All these conditions define the ion-to-neutral arrival rate ratio of carbon and nitrogen, and the ion and neutral particle energy distribution. Previous studies on single magnetron sputtered FL CN_x films employed an up to 20-times-higher ion bombardment (by means of flux density) as compared to this study, while the pressure, neutral flux, and ion energy was kept at a comparable level.[10] Here, the lower ion flux density gives rise to a reduced average energy per incorporated particle by lowering the ion-to-neutral arrival rate ratio, while keeping the ion energy constant at approximately 25 eV. The influence of a slightly higher ion energy of approximately 40 eV on the structure evolution and properties is also considered.

We report in this article on the formation and bonding structure of FL structures in CN_x and their impact upon the mechanical properties of thin solid films. The growth of this material is found to change significantly with an increase in the availability of nitrogen and the incident ion energy. For films grown at a low ion energy (25 eV), the radius of curvature of basal planes is inversely proportional to N_2 partial pressure and varies from a multishell onion-like structure (with approximately 0.35-nm radius for the smallest shells) to almost straight graphitic planes containing 17 at. % N as grown in a pure N_2 discharge. The multishell FL structure shows an increased hardness and elastic modulus, while maintaining a relatively high hardness-to-modulus ratio, which gives rise to remarkable elasticity and toughness. A rise in ion energy by just 15 to 40 eV leads to a completely different mechanical response. The films are still very elastic, but exhibit an up-to-threefold increase in hardness and modulus, while the long-range order in the multishell FL microstructure is decreased.

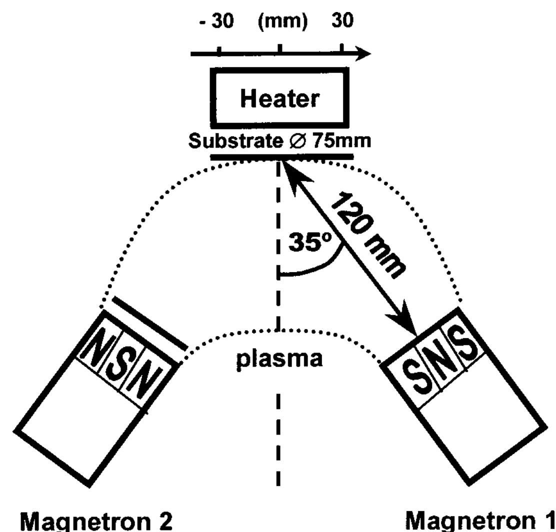

FIG. 1. Schematic of the sputtering system, showing the substrate position and indicating the coupled configuration of the two magnetrons. For the experiments, magnetron 1 was operated with a C target and magnetron 2 was idle. The scale at substrate position defines the location of the individual probes in Fig. 2.

EXPERIMENTAL DETAILS

Experimental setup and film growth

FL CN_x films were deposited by dual dc unbalanced reactive magnetron sputtering in a UHV system with a base pressure of 1×10^{-7} Pa. A 99.99% pure pyrolytic graphite was sputtered from one single target (75-mm diameter) in a mixed Ar/N_2 discharge (99.9999% purity). The plasma was confined in front of the substrate by a coupled magnetic field generated from a second magnetron. Unbalanced magnetrons were employed with a magnetic flux from the outer poles of 5.6×10^{-4} Wb and the inner poles 3.8×10^{-5} Wb. The biased substrate holder was rotated and resistively heated from the reverse side. It was mounted at the point of focus in between the two magnetrons at a distance of 120 mm. A schematic diagram of the experimental apparatus is shown in Fig. 1.

The total pressure was kept constant at 0.4 Pa, which was measured with a capacitance manometer, and the Ar/N_2 ratio varied from 0 to 1. The substrates were held at 450 °C with a resistively heated graphite heater, which was calibrated with a k-type thermocouple at the substrate position. The magnetrons were regulated at a constant discharge current of 400 mA, with a resulting voltage that varied from 525 V, in a pure Ar discharge, to 465 V in a N_2 discharge.

The films were deposited at bias voltages of -25 and -40 V for 3 h onto (100) Si wafers, ultrasonically cleaned in acetone and isopropanol in sequence prior to deposition. These conditions resulted in a film thickness of approximately 400 nm. The samples for transmission electron microscope (TEM) plan views were prepared by a 20 min deposition onto freshly cleaved NaCl wafers.

Downloaded 17 Mar 2003 to 148.6.104.15. Redistribution subject to AIP license or copyright, see http://ojps.aip.org/japo/japcr.jsp

During deposition, the stress development was recorded by monitoring the curvature of 3 inch Si wafer with a k-SA MOS system (k-Space Associates). A laser is split into an array (4×4) of spots and reflected from the substrate into a CCD detector. The spot spacing is recorded in two perpendicular directions, and from this the radius of curvature is determined. The total stress in the film can be calculated from Stoney's equation for a known substrate thickness and biaxial modulus combined with a known film growth rate. This method is accurate assuming a film significantly thinner than the substrate, and that stresses in the film do not exceed the yield strength of the Si substrate ($\approx$7 GPa).[11]

Plasma characterization

The structure and properties of CN_x is extremely sensitive to parameters such as ion flux and ion energy.[10] Therefore, it is crucial to monitor the plasma parameters for the growth conditions in order to determine the energy and number of arriving ions. The saturation ion flux was measured prior to deposition at -100 V by an array of flat plasma probes with an area of 0.5 cm^2 each. Seven probes were evenly distributed at the substrate position, forming a line between the two targets in order to study the radial distribution of the ion flux. The self-floating potential was measured on the center probe. The surrounding holder was kept at measuring potential in order to minimize edge effects.

A small tungsten wire probe (∅ 0.2 mm; length 5 mm) was used to record the $I-V$ curves at the substrate position. The voltage was swept from -160 to $+20$ V and the resulting probe current was measured. From these curves, the plasma potential was derived as the potential at the inflection point in between the ion-dominated part and the electron-dominated part, given by

$$V_{\mathrm{pl}}=d^2V/dI^2=0. \tag{1}$$

Assuming homogeneous plasma around the probe and a Maxwell–Boltzmann energy distribution of the electrons in the plasma, their temperature and density can be derived by knowing the area of the probe (A_{pr}) by the following equations:[12]

$$T_e=\frac{e}{k}\,\frac{\int_{V_{fl}}^{V_{pl}} I_{(V)}dV}{I_{(V_{\mathrm{pl}})}}, \tag{2}$$

$$n_e=\frac{I_{(V_{\mathrm{pl}})}}{A_{pr}}\sqrt{\frac{2\pi m_e}{e^2kT_e}}. \tag{3}$$

Film analysis

The substrates for thickness measurements were masked with spots of a isopropanol/TiO_2-powder mixture across the diameter prior to deposition. After deposition, the TiO_2 can be easily wiped off, and the resulting step was measured in the center, and at 15 mm and 30 mm towards the perimeter of the sample holder with a surface profilometer (DekTak 3030, Veeco Instruments) to determine the growth rate and homogeneity across the holder. Each step was measured four times to minimize systematic errors.

Elastic recoil detection analysis (ERDA) was used to determine the areal density of elements present in the films. The films were exposed to a 35 MeV Cl^{7+} ion beam under an incidence angle of 15°. The atomic number and energy of the forward sputtered particles were analyzed by an ionization chamber (in the case of H by a semiconductor detector) in order to determine the energy (E) and mass (Z) of each forward sputtered particle. The areal densities of each element were calculated from integrating the resulting $E-Z$ chart. From the sum of the areal densities and the growth rate follows the mass density of the films. The energy of the particles scales with the escape depth from the analyzed volume and, therefore, allows compositional depth profiles to be derived, since the relation of the different areal densities corresponds directly to the elemental composition.[13]

The chemical bonding structure in the near-surface region was analyzed with a VG Microlab 310F combined Auger electron spectroscopy and x-ray photoelectron spectroscopy (XPS) system. After deposition, the samples were analyzed by XPS using a non-monochromated Mg K_α (1253.6 eV) x-ray source and a hemispherical electron energy analyzer without any initial sputter cleaning. The energy analyzer was set such that the Au ($4f_{7/2}$) was recorded with a full width at half maximum (FWHM) of $\approx$0.9 eV. For comparison to ERDA, the composition of the films was estimated by the peak area ratios of the C1s and N1s core level spectra.

A Digital Instruments Nanoscope IIIa atomic force microscope (AFM) in tapping mode was used in order to determine the surface roughness parameters of the films. The RMS value was determined from a $1\times1\ \mu m^2$ area scanned at a resolution of 512×512 pixels.

To evaluate the mechanical response of the films, nanoindentation experiments were carried out using a Triboscope® (Hysitron Inc.) connected to the AFM. The combination of the two systems gives the unique possibility to scan the surface, before and after the indent is made, in order to image the surface topography. This allows a check for obstacles on the surface, before indentation and imaging of the residual indent, to evaluate pile-up effects on the edges or a sinking of the surrounding area. The Hysitron transducer has a force resolution of 0.2 μN and a displacement resolution of 0.5 nm, which creates indentation curves on the nanometer scale. The system was equipped for most experiments with a cube corner diamond tip (three-sided pyramid with 90° total included tip angle, $E=1141$ GPa, $\nu=0.07$). This tip is sharper than a Berkovich (142.3° total included tip angle), which leads to a higher stress concentration under the indenter, so that the elastic–plastic transition occurs at lower loads and the resulting stress strain field is more elongated in the film. Hence, the film properties dominate the load displacement curves at higher loads as compared to Berkovich indents.[14,15]

A lack of plastic deformation makes the indentation hardness and modulus analysis after Oliver and Pharr rather dubious, since this theory was developed for plastically deforming materials like metals.[16] In order to induce more plastic deformation during indentation, even for extremely shallow indents, the stress concentration under the indenter must

Downloaded 17 Mar 2003 to 148.6.104.15. Redistribution subject to AIP license or copyright, see http://ojps.aip.org/japo/japcr.jsp

be increased. This can be done by changing the geometry from a conventional three-sided Berkovich-shaped diamond indenter with a tip angle of 142.3° to a pointier tip, like a cube corner with an tip angle of 90°. Another effect that increases the stress concentration for a cube corner indenter is the typically lower value of the tip radius in comparison to a Berkovich indenter. The tip radii for both types of indenters were estimated by purely elastic indents in amorphous SiO_2 with a given reduced modulus of 69.9 GPa. The indents were modeled as a Hertzian contact between a flat surface and a perfectly stiff, round indenter.[17] This is a legitimate assumption given the large difference between the elastic moduli of diamond and amorphous SiO_2. It has to be kept in mind that the tip of an indenter is not spherical, but is rather a kind of truncated cone, and the radii derived from the Hertzian contact can be used as guidelines. The radius of the effective tip roundness was 80 nm for the cube corner and 130 nm for the Berkovich diamond used in this study. Elastic–plastic indentations were made in amorphous SiO_2 as well in order to take the real shape of the cube corner diamond tip into account in form of an tip-area-function as suggested by Oliver and Pharr.[16] The tip area function, representing the depth-area relation, was derived from these indents at a contact depth range from 5 to 380 nm. The thermal drift was recorded before each indent at a constant load of 2 μN and taken into account.

A series of indents ranging from 125 μN up to 7.5 mN were made in each film. A power law was fitted from 40% up to 95% of the unloading part to get the compound stiffness from a straight line fitted to the upper part. From the stiffness the indentation hardness and reduced Young's modulus of the film–substrate system were calculated using the method described by Oliver and Pharr.[16] The resulting values, representing the transition from substrate-dominated to film-influenced response, were fitted with a function suggested by Korunski *et al.*[18] giving the uninfluenced hardness and modulus values of the film.

The microstructure of the films was characterized by high-resolution (HRTEM) using a Philips CM 20 UT transmission electron microscope operated at 200 kV with a point resolution of 0.19 nm. Plan-view samples were prepared by depositing approximately 50-nm-thick films onto freshly cleaved NaCl wafers. After deposition, the films were immediately floated off in deionized water, rinsed in three stages, and collected onto Cu microscopy grids for examination. This method offers a large electron transparent area suited for investigation. TEM cross sections were prepared by low-angle and low-energy ion-beam milling to limit the thickness of the amorphized surface layer.[19]

RESULTS

Plasma characterization

The energy and radial distribution of species incident on the substrate is defined by the confinement of the plasma generated during the magnetron discharge and the applied external bias voltage. Generally, the plasma produced by the unsaturated magnetic field lines of a single unbalanced magnetron is fairly focused at the plane of the substrate and thus forms a plume.[10] In order to decrease the ion current at the center of the substrate holder and to homogenize the plasma across the diameter of the substrate, the plasma was trapped in a mirror magnetic field generated by a second magnetron (Fig. 1). The magnetic field lines of the two magnetrons were connected due to the coupling of the adjacent magnetic poles. Therefore, the electrons are gyrating along the field lines, and due to the quasineutrality of plasma, the ions follow so that the plasma forms an arch in between the two targets.

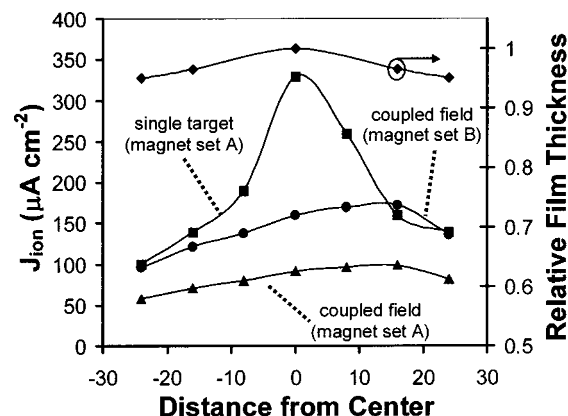

FIG. 2. Saturation ion flux measured by flat plasma probes as a function of the position on the sample holder for different magnet configurations; with a single target or coupled fields and a magnet set A and B (magnetic flux density is larger for set B). The relative thickness distribution is also shown.

The ion flux, as an indicator for the plasma density, was measured across the substrate holder for two different sets of magnets and compared to the distribution from a single target, as shown in Fig. 2. It can be seen that the plasma, described by the saturation ion flux, for a single magnetron is very much focused at the center of the holder. The large gradient towards the edges of the holder makes it difficult to state precise values for the crucial ion bombardment at certain substrate positions. One advantage of a two-magnetron configuration in a coupled mode is the homogenization of the plasma across the holder. Thus, precise plasma properties can be assigned to a significantly larger area. Combined with a homogeneous neutral flux, represented by the relative thickness in Fig. 2, this makes for comparable growth conditions across the diameter. On the other hand, the trapping of the plasma in the coupled magnetic field leads to a decreased ion current. This was compensated for by a different set of magnets with a higher magnetic flux as shown in Fig. 2, where magnet set "A" comprises the weaker magnets. The magnet set "B," giving a higher flux, was then used for the film depositions.

The properties of the plasma, such as ion and electron temperature, and plasma density and composition, are defined by the discharge conditions, which include geometry, discharge current, gas pressure and composition, sputtered material, and magnetic field and electric field characteristics. The gas composition was varied in this study, and its effect on the plasma properties is shown in Table I. The electron temperature was estimated to be approximately 0.5 eV independent of the gas composition. This low value, even for a

Downloaded 17 Mar 2003 to 148.6.104.15. Redistribution subject to AIP license or copyright, see http://ojps.aip.org/japo/japcr.jsp

TABLE I. Variation of the discharge voltage, floating potential, plasma potential, electron density, and saturation ion flux as a function of the gas composition during magnetron sputtering from a C target in a Ar/N_2 discharge ($I_{discharge}$=400 mA; p_{total}=0.4 Pa).

N_2 fraction	$U_{discharge}$ (V)	$V_{floating}$ (V)	V_{plasma} (V)	n_e (10^9 cm^{-3})	J_{ion} ($\mu A\, cm^{-2}$)
1	465	−7.8	0.6	4.5	150
0.66	487	−7.7			140
0.5	504		0.9	5.0	
0.33	508	−8.9			150
0	525	−8.0	1.7	5.6	160

sputtering plasma, combined with a self-floating potential of around −8 V can be attributed to the fact that the substrate was situated on the edge of the arch-shaped plasma. This also affects the entire $I-V$ curve. The nonhomogeneous plasma density normal to the substrate leads to an overestimation of the current saturation regions, since a higher negative/positive potential attracts ions/electrons over larger distances compared to the currents around the plasma potential. It can, however, be concluded that the plasma potential is approximately 1 V, representing an electron temperature of 0.5 eV and a corresponding electron density of approximately 5×10^9 cm^{-3}. No significant variations in the plasma dependent on changes in the gas composition were observed. The plasma trapped in the coupled field of the two magnetrons results in a saturation ion flux of approximately 150 $\mu A\, cm^{-2}$.

The discharge was maintained by a constant current of 400 mA, and the resulting voltage needed to sustain the given current is shown in Table I. Its magnitude is defined by the primary electron yield of particles in the gas phase and the secondary electron yield of the target material, and therefore it represents the change in gas and target chemistry with a variation in N_2 fraction.

Growth

The growth rate varied between 0.035 and 0.052 ±3% nm s^{-1} for the given deposition conditions, with only a weak dependence on the N_2 fraction, as shown in Table II. This table also gives the incorporation rate, representing the number of particles incorporated per square meter per second, which was calculated from the areal densities as measured by ERDA and the deposition time. The highest values are observed for higher N_2 fractions, and there is a distinct decrease with a reduction of the N_2 fraction in the discharge gas, with a minimum for films grown in a pure Ar discharge. This dependence is less pronounced for the films grown with −40 V bias. For a comparison between the number of particles incorporated and the number of ions impinging at the growing surface, the ion arrival rate is also shown in Table II. It is derived from the saturation ion flux (Table I), assuming that only single charged ions bombard the growth surface.

Composition

Figure 3 shows the effect of the N_2 fraction in the discharge gas and the applied bias voltage on the N concentration in the film. The N concentration is already 13 at. % for a

TABLE II. Film density, growth rate, incorporation rate, and ion arrival rate, depending on the N_2 fraction and bias voltage. The ion arrival rate was derived from the ion saturation flux measured by a flat plasma probe.

Bias	N_2 fraction	Density ($g\, cm^{-3}$)	Growth rate (10^{-10} m s^{-1})	Incorporation rate (10^{14} s^{-1} cm^{-2})	Ion arrival rate (10^{14} s^{-1} cm^{-2})
−25 V	1[a]	2.8	0.49	6.7	9.5
	0.92[a]	2.4	0.52	6.1	
	0.84[a]	2.4	0.45	5.3	
	0.67	2.3	0.42	4.8	8.6
	0.58	2.4	0.44	5.2	
	0.5	2.4	0.39	4.5	
	0.42	2.4	0.37	4.4	
	0.33	2.3	0.37	4.1	9.4
	0.16	2.4	0.36	4.1	
	0.08	2.1	0.37	3.8	
	0	0.6	1.6	3.4	10.0
−40 V	1	2.3	0.4	4.5	9.5
	0.66	2.4	0.41	4.8	8.6
	0.5	2.1	0.44	4.4	
	0.33	2.1	0.44	4.5	9.4
	0	0.4	1.92	3.5	10.0

[a]Hydrogen contamination.

Downloaded 17 Mar 2003 to 148.6.104.15. Redistribution subject to AIP license or copyright, see http://ojps.aip.org/japo/japcr.jsp

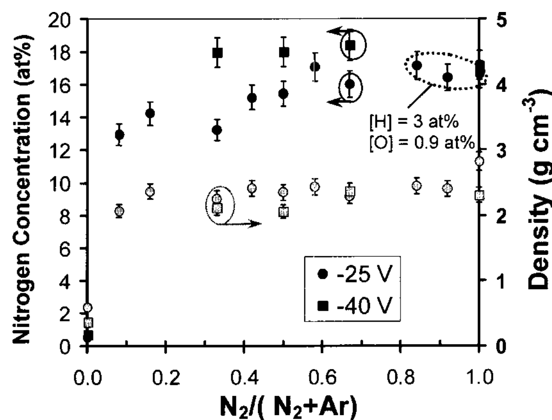

FIG. 3. Film density and N concentration, as determined by ERDA, versus N_2 fraction in the discharge gas and for different substrate bias values of -25 V and -40 V. Three of the films grown at the highest N_2 fraction and -25 V bias showed an elevated impurity level, as indicated.

N_2 fraction of just 0.08 (the lowest one used) and -25 V bias. For higher N_2 fractions, there is only a slight increase in N content in the film, and it saturates at 16–17 at. % for a bias of -25 V and a N_2 fraction of greater than 0.5. If -40 V bias is applied during deposition, the N content in the films is stable at approximately 18 at. %, and no noticeable dependence on the N_2 fraction is observed. The total impurity level in the N containing films regarding the oxygen and hydrogen uptake, due to the dissociation of water in the residual gas, is negligible, being below the detection limit of 0.1 at. % for O and 0.5 at. % for H. This low impurity level is a direct effect of the low base pressure of $<1\times10^{-7}$ Pa in the system prior to deposition. However, three of the nitrogen containing films show a significantly higher H and O uptake, as indicated in Fig. 3, which might be due to hydrocarbon contamination of the new pyrolytic graphite target after target change.

The results of the XPS compositional analysis, compared to those determined by ERDA, are plotted in Fig. 4. In comparison, XPS overestimates the N concentration for higher N_2 fractions by as much as 30%, while underestimating it by approximately 20% for films grown at lower N_2 fractions.

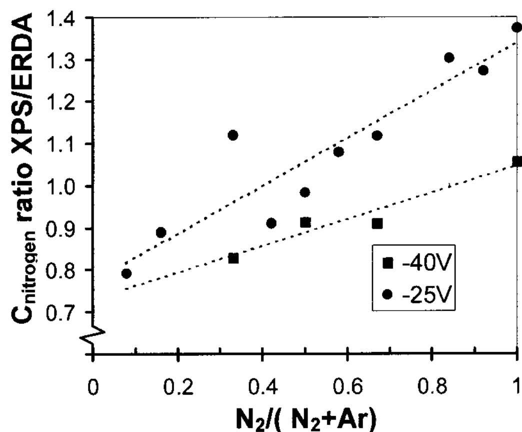

FIG. 4. Ratio of N concentrations determined by the peak area ratio in XPS and area density in ERDA plotted for the two sample series.

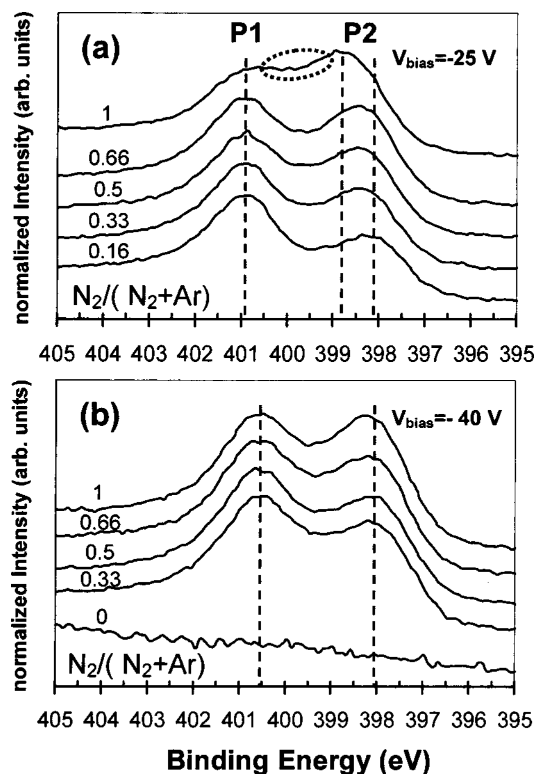

FIG. 5. XPS N1s core-level spectra for CN_x films grown at a range of N_2 fractions and substrate bias values (a.) -25 V and (b.) -40 V, respectively. The apparent merging of P2 towards P1, in the spectra taken at -25 V and a N_2 fraction of 1, is caused by an additional peak due to contamination.

This huge difference is attributed to surface effects, since the depth of information for XPS is just a few atomic layers. One way to explain this situation is the adsorption of atmospheric gases, such as N_2, O_2, or H_2O. These gases can react with the CN_x surface, especially near N sites, and therefore can increase the XPS N1s peak area by adding, for example, N–O bonding-type contributions. The reactivity of the CN_x surface layers depends on their structure. A standing graphitic basal plane in a turbostratic structure is more reactive at the edge sites as compared to the surface sites of a more three-dimensional FL structure with closed shells. Hence, the N1s peak pattern is more or less influenced, leading to a variation in the apparent composition determined by XPS. ERDA, on the other hand, determines the bulk composition by the areal densities of the components.

Chemical bonding structure

No major chemical shift or changes were observed for the XPS C1s peak within the resolution limits of the system. A slight unsymmetrical broadening, however, could be resolved. Figure 5 shows the XPS N1s core level spectra for CN_x films grown at a range of N_2 fractions and substrate bias values of (a) -25 V and (b) -40 V, respectively. The spectra were normalized to the same maximum intensity and a Shirley-type background was subtracted. Up to four spectral contributions can be resolved by fitting a Gaussian line shape.[20] Only two give a significant contribution at binding energies of approximately 400.7 eV (P1) and 398.3 eV (P2). No change in peak position is observed for most of the peaks. Only P2 for the sample series grown at -25 V bias

Downloaded 17 Mar 2003 to 148.6.104.15. Redistribution subject to AIP license or copyright, see http://ojps.aip.org/japo/japcr.jsp

shows a shift from about 398.6 eV for the film grown at a N_2 fraction of 1, down to 398.1 eV for the film grown at a N_2 fraction of 0.08. This shift can be caused by a charge transfer with respect to the atomic nucleii and/or a different charge compensation response of the surrounding material after the photoelectron was removed.

The two distinctive XPS N1*s* peaks suggest that nitrogen is bonded in at least two different chemical environments. The assignment of these two contributions diverge somewhat in the literature; for a review see Ref. 21. It is fairly well established that P1 can be assigned to N bonded substitutionally for C in a graphitic sheet.[20,22] The origin of P2, however, is still under discussion. There are a variety of different assignments and calculations to be found in the literature. Most recent studies reinforce the idea that P2 can be connected to N bonded in a pyridine-like manner into a graphitic network and/or N triple bonded to just one carbon atom, especially since there is no evidence for larger quantities of sp^3 hybridized carbon by, for example, x-ray absorption/emission spectroscopy.[23] Another common interpretation, also quite often found in the literature, is the assignment to N bonded in a partially sp^3 hybridized C matrix.[20,22,24,25]

The FWHM of approximately 2 eV for each peak, which is higher than the resolution of the system (<1 eV), suggest that the peak pattern carries information of an inherent broadening mechanism, caused by a scattering of one chemical state over a range of about 1 eV. This can be understood by differences in the charge distributions for one type of chemical bonds due to long-range interactions,[26,27] such as the curvature of the graphitic sheets or edge effects.

It is postulated that the variety of curvatures and cross-linkage observed in FL CN_x leads to an anisotropy in charge distribution due to the accumulation of the N lone-pairs on the side of positive curvature. In turn, this affects the binding energy for the N1*s* electrons involved and is detected as a peak broadening. Also, the location of the N emitting a core electron, within a CN_x sheet, is important for the peak broadening. The lost charge can only be compensated from inside the same graphitic sheet, due to a much lower in-plane resistivity. If the N atom is situated closer to edges, this process is hampered, leading to a small positive effective charge on the nuclei that therefore increases the binding energy slightly.

The peak area ratio is plotted in Fig. 6. A clear trend can be resolved with an increasing peak area ratio of P2 compared to P1 as a function of N_2 in the discharge. At the higher ion energy (40 eV), the peak ratio is slightly higher for films grown at the same N_2 fraction.

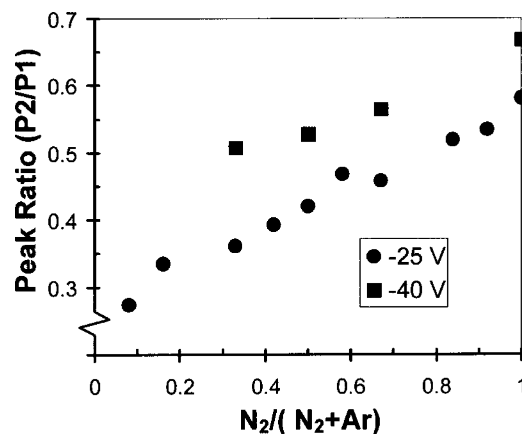

FIG. 6. XPS peak ratio for the sample series made at -25 V and -40 V substrate bias, derived from the area ratio of the two major contributions (P1/P2) of the XPS N1 core level spectra, as fitted by a Gaussian peak shape combined with a linear background.

Figure 7 shows representative plan-view transmission electron micrographs of the as-deposited films. The FL CN_x, consisting of bent and intersecting graphitic basal planes with an interplanar lattice spacing of ~ 0.35 nm, is apparent. The main difference between the microstructures of the films is the degree of curvature, extent, and alignment of the sheets. The films grown at a lower N_2 fraction at both bias voltages exhibit the most pronounced FL structure, with small radii of curvature and frequent intersecting of planes, much like in a fingerprint. For an increase in N_2 fraction, the structure changes, in case of a lower bias voltage towards a more graphitic structure, with straight, well-aligned planes. For a 15-eV-higher ion energy, the extension of the planes and their alignment decreases with an increase in N_2 fraction; for a pure N_2 discharge the structure is almost amorphous. Plan views of the films grown without N_2 reveal a completely amorphous structure (not shown).

The most outstanding structures were observed for very low N_2 fractions and a low bias voltage, as shown in Fig. 8. At these growth conditions, the FL sheets form well-aligned, multilayered spherical features, so called "nano-onions,"[3] with an inner-shell diameter of approximately 0.7 nm and successive shells at a distance of ~ 0.35 nm up to a diameter of 5 nm. The entire film consists of these nanometer-sized, multi-walled CN_x half-dome-like shells. The micrograph was taken at a tear edge of a floated-off film, and shows a crack propagating along the outer shells of the individual features, indicating their substantial internal cohesive strength.

Cross-sectional micrographs were made by ion milling to clarify that the structures seen in the plan-view micrographs are representative of the bulk of the films and not just a nucleation effect. Figure 9 is a typical example from a film

Microstructure

The films grown at -25 V have RMS roughness values, as measured by AFM, ranging from 0.8 to 4.9 nm depending on the N_2 fraction (see Table III). The -40 V sample series is somewhat smoother, with rms roughness values of approximately 0.2 nm. Not surprisingly, the films grown in a pure Ar discharge have about an order of magnitude higher RMS values, corresponding to their under-dense structure.

TABLE III. Rms surface roughness, determined from an AFM $1\times1\ \mu m^2$ surface scan in noncontact mode, depending on N_2 fraction and bias voltage.

N_2 fraction	0	0.3	0.5	0.6	1	
Rms	-25 V bias	51.4	0.8	1.5	4.6	4.9
nm	-40 V bias	16.2	0.2	0.2	0.2	0.4

Downloaded 17 Mar 2003 to 148.6.104.15. Redistribution subject to AIP license or copyright, see http://ojps.aip.org/japo/japcr.jsp

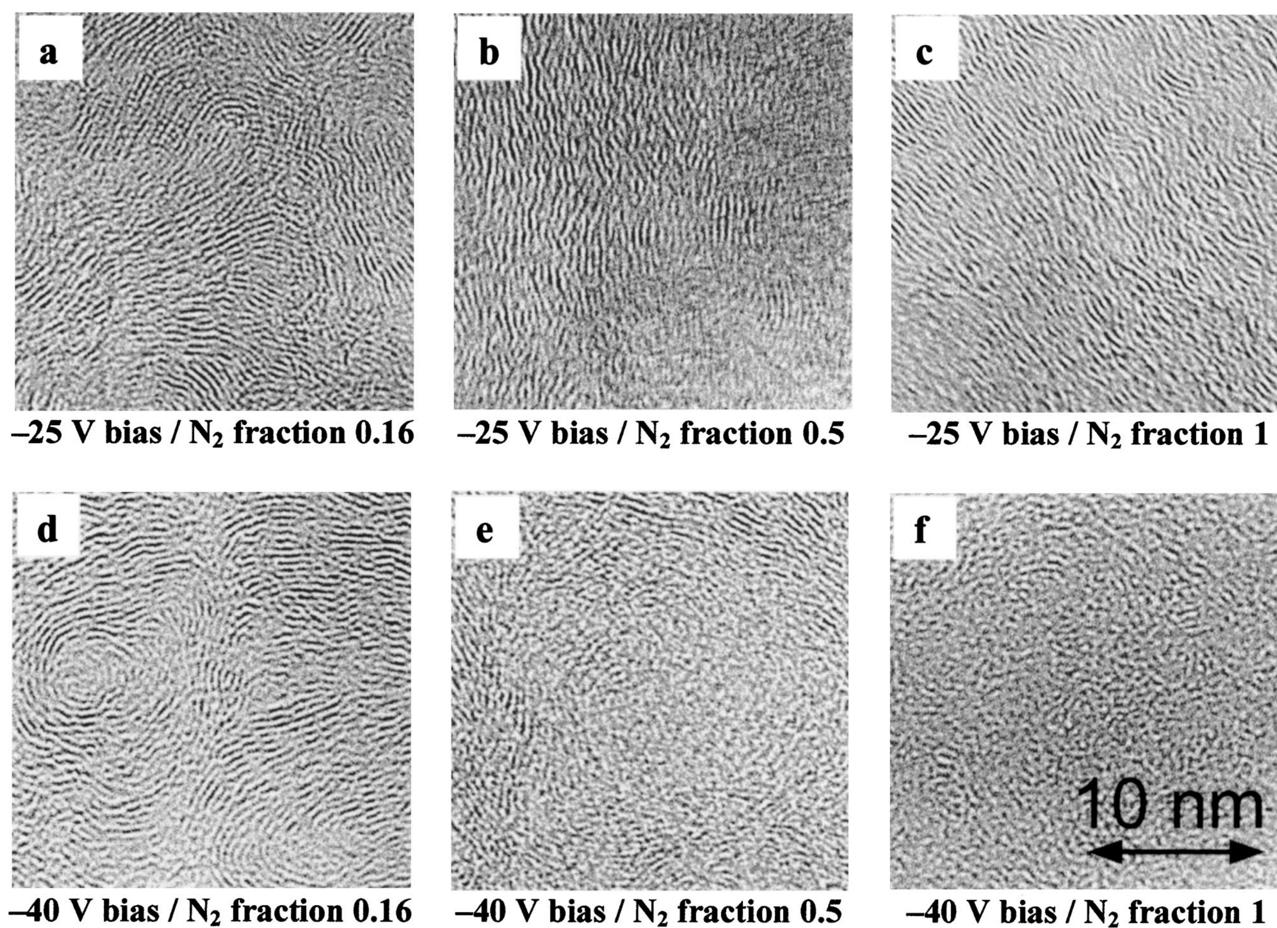

FIG. 7. HRTEM plan-view micrographs of CN_x films of floated-off specimens from sample series deposited at N_2 fractions of 0.16, 0.5, and 1, and -25 and -40-V biasas, respectively.

grown at a N_2 fraction of 0.16 and -25 V bias, revealing a homogenous microstructure throughout the 400-nm film thickness (~150-nm shown). One can conclude that the plan-view micrographs shown in Fig. 7 are representative of the entire respective films.

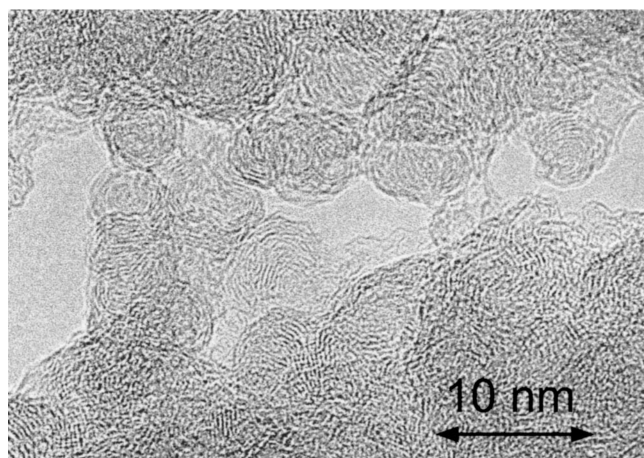

FIG. 8. HRTEM plan-view micrograph, taken at the fracture (tear) edge of a floated-off film, grown at a N_2 fraction of 0.1 and -25-V bias. The thickness requirement for imaging single features is met along the edge and single nano-onions can be resolved, consisting of 7–10 concentric hemispherical shells at a ~0.35-nm lattice spacing.

Mechanical properties

Dense CN_x material is known to be very elastic, which causes some difficulty for the indentation analysis of thin films, as discussed in the experimental section and in Ref. 28. The films examined by nano-indentation were grown to a thickness of approximately 400 nm.

Figure 10 shows load displacement curves for a film grown at a N_2 fraction of 1 and at -25 V bias for the Berkovich and cube corner indenters at a variety of loads. The cube corner indents are characterized by a much larger displacement at the same loads and a higher fraction of plastic work of indentation, represented by the area enclosed between the loading and unloading part of the curve. At loads up to 10 mN, the response is clearly influenced by the substrate. It also has to be noted that a stick-slip effect occurs for the cube corner indenter at larger displacements, as seen for the approximately 500 nm deep indent, due to friction between the indenter and the displaced material. Another effect of a cube corner at higher loads is that cracking in the film or substrate can occur for less resilient materials. However, the advantage of cube corner geometry lays in low-load and low-displacement indents as needed for thin film testing. Whereas the displacement and therefore the load have to be decreased in order to minimize the substrate influence. At lower loads

Downloaded 17 Mar 2003 to 148.6.104.15. Redistribution subject to AIP license or copyright, see http://ojps.aip.org/japo/japcr.jsp

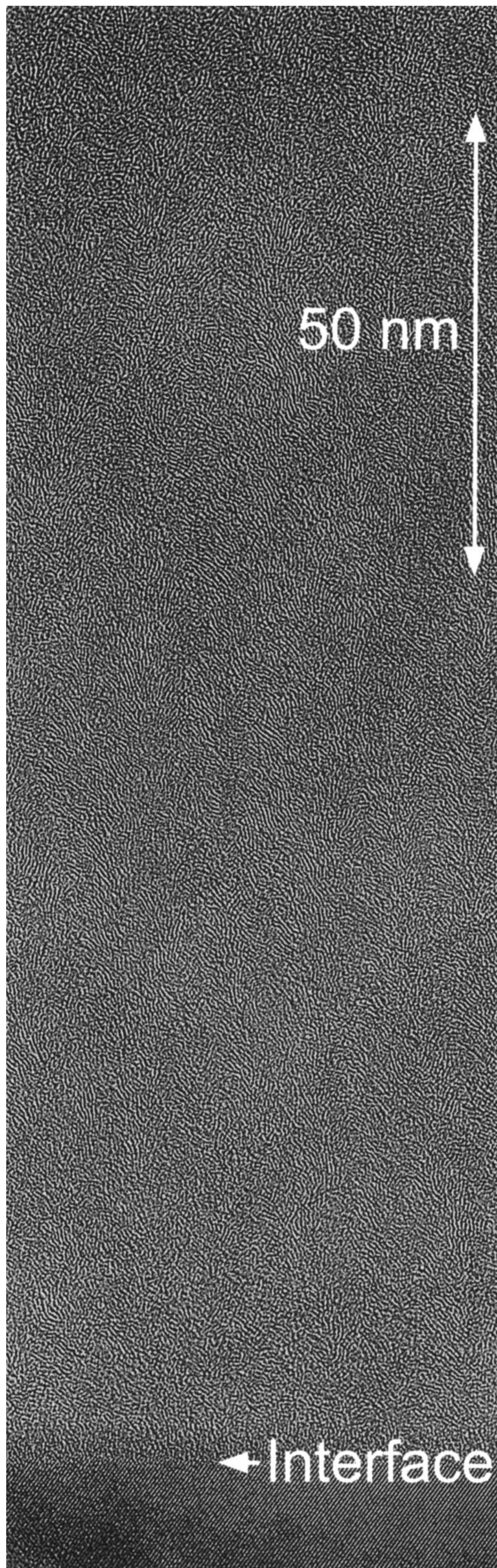

FIG. 9. HRTEM cross-sectional micrograph of a film grown at −25 V and a N_2 fraction of 0.1 prepared by ion-beam milling, showing the homogeneity of the film structure throughout the volume.

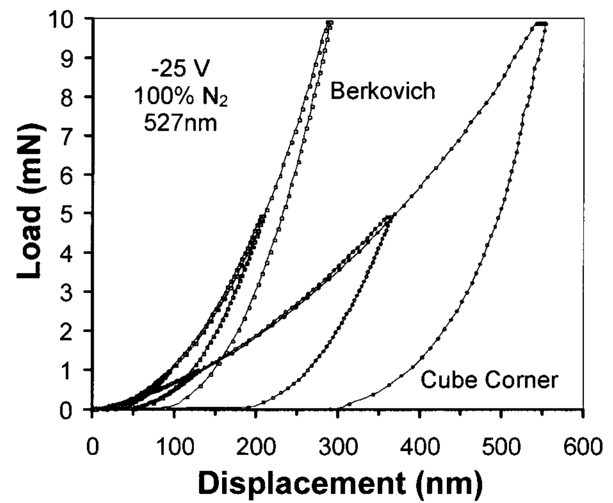

FIG. 10. Nano-indentation load–displacement curves for indents made with Berkovich or cube corner diamond indenters at loads of 1, 5, and 10 mN for a film grown −25 V bias and a N_2 fraction of 1.

(<1 mN), the indents made with a cube corner indenter still show a significant plastic work of indentation, while the Berkovich indents are purely elastic, which allows Oliver and Pharr analysis only in the former case.

Figure 11 shows the load–displacement curves obtained with a cube corner indenter from a CN_x film (N_2 fraction 0.16, bias −25 V), and some crystalline and amorphous reference materials. The indents in CN_x exhibit a large displacement of 75 nm, even deeper than for amorphous SiO_2 but, remarkably, with a next-to-total elastic response. In fact, CN_x behaves extremely elastically compared to sapphire, silica, and silicon, with a remarkable elastic recovery from displacements as large as 100 nm. To achieve total elasticity for, for example, sapphire, the load has to be reduced to 100 μN, giving only 5-nm displacement.

Indentation in CN_x to such depths without yielding suggests that the massive elastic deformation has to be accom-

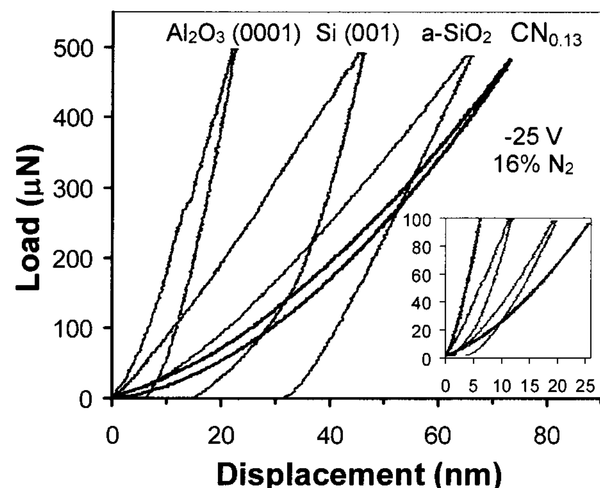

FIG. 11. Nano-indentation load–displacement curves with cube corner diamond indenter in a 400 nm thick CN_x film (−25 V bias, N_2 fraction=1) on a Si substrate compared to bulk materials of Al_2O_3 (0001), Si (001), and amorphous SiO_2 at loads of 500 and 100 μN (inset), respectively.

Downloaded 17 Mar 2003 to 148.6.104.15. Redistribution subject to AIP license or copyright, see http://ojps.aip.org/japo/japcr.jsp

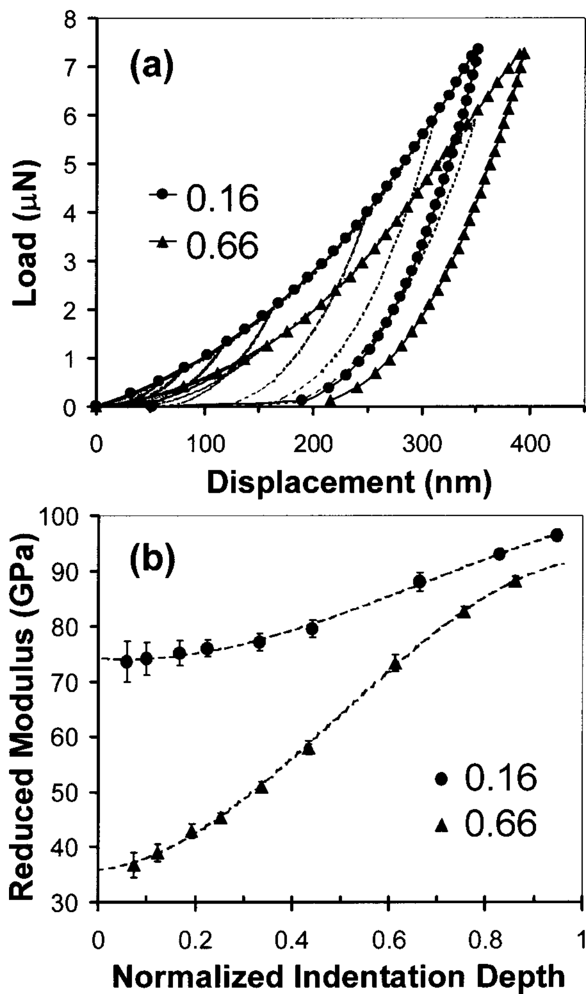

FIG. 12. (a) Comparison of nano-indentation load–displacement curves of two CN_x films grown at -25 V, and N_2 fractions of 0.16 and 0.66, done with a cube corner diamond indenter for a range of loads. (b) Reduced modulus values of the film–substrate composite plotted over the normalized indentation depth for a range of loads. The data are fitted with a function, suggested by Korunsky *et al.*,[18] to derive the film-only values.

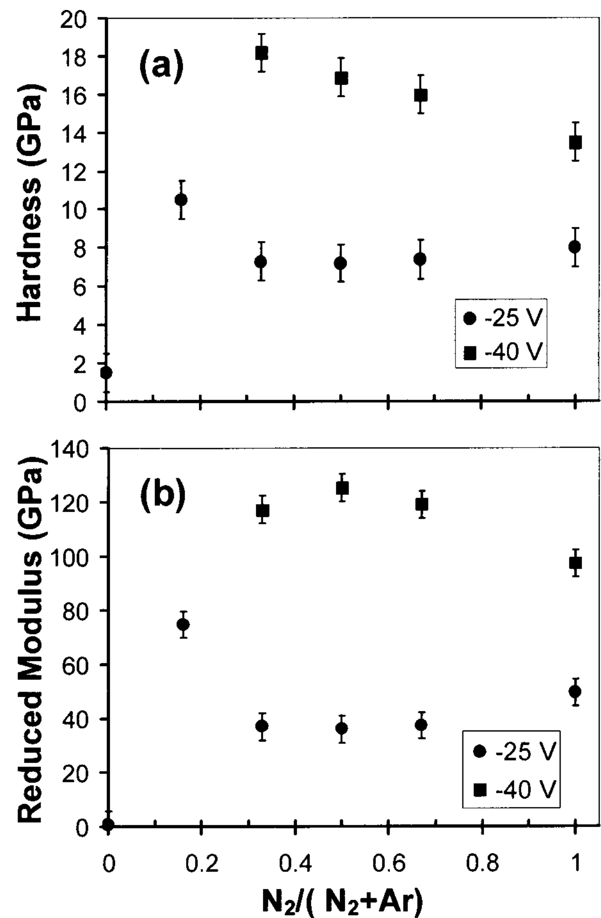

FIG. 13. Film-only hardness (a) and modulus (b) values, depending on the N_2 fraction and substrate bias, of the $-25/-40$ V sample series as derived by the method shown in Fig. 12(b).

modated in a comparatively large stress field under the indenter. For thin films, this stressed volume readily extends into the substrate and therefore the load–displacement curves, even at very low loads, will show a combined substrate–film response.[29] Very shallow, below 20 nm, indents would be required to make the substrate influence negligible. Besides the difficulties in analyzing these fully elastic intents with conventional methods, the surface roughness has peak-to-valley values of the same order of magnitude (Table III), which results in a large scatter in the load–displacement curves, depending on the position of the indent with respect to surface features.

In order overcome the problems in evaluation of the indentation response and to obtain the film only hardness/modulus values, the model suggested by Korunsky *et al.*[18] was employed:

$$H_C = H_S + \frac{H_F - H_S}{1 + k\beta^2}, \tag{4}$$

with k a constant, composite hardness (H_c), substrate hardness (H_s), and film hardness (H_f). β is the indentation depth, (δ) normalized to the film thickness (t):

$$\beta = \frac{\delta}{t}. \tag{5}$$

This model is based on the total work of indentation for a given sized indent done by the indenter on the film and the substrate. This means that the energy is dissipated in the deforming volumes of substrate and film. The ratio between those two volumes represents the transition from a film- to substrate-dominated response. Other parameters, such as possible delamination at the interface and cracking in the film, are described by the fitting constant k.

For the evaluation of the film-only reduced modulus, the same equation with moduli instead of hardness was used. A series of indents for loads ranging from 7.5 mN down to 125 μN were made on each film, resulting in a β value from ≈ 1 down to ≈ 0.05, depending on the indentation response of the particular film. Figure 12 shows an example of such a series of indents (a) combined with the resulting modulus and the corresponding fit (b) for two films grown at -25 V bias and N_2 fractions of 0.16 and 0.66. The correlation coefficient of the fit in both cases was >0.99. For $\beta \gg 1$, the modulus value represents the substrate-only response and was fitted to 154 GPa, which is in good agreement with the

Downloaded 17 Mar 2003 to 148.6.104.15. Redistribution subject to AIP license or copyright, see http://ojps.aip.org/japo/japcr.jsp

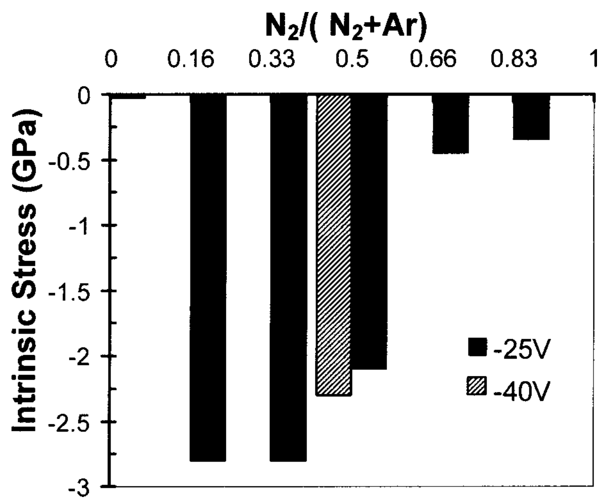

FIG. 14. Compressive intrinsic stress for the sample series deposited at −25 V bias as a function of N_2 fraction in the discharge. One film grown at −40 V substrate bias is shown for comparison.

modulus of silicon. The film-only elastic moduli were estimated to be 74 GPa and 37 GPa, respectively, for $\beta=0$. As one can see in Fig. 12, indents with a displacement even as shallow as 5% of the film thickness are still influenced by the substrate, especially for the "softer" films.

The same procedure was repeated for a variety of films grown at different N_2 fractions, at bias voltages of −25 V and −40 V, in order to calculate the reduced modulus and hardness: Fig. 13 summarizes the results. The films grown at −25 V bias have a reduced modulus around 40 GPa, except that the film grown at a N_2 fraction of 0.16 exhibits a modulus of up to 75 GPa. Surprisingly, a 15 V change in bias to −40 V causes a dramatic increase in the modulus values of up to 125 GPa. The films grown at −25 V have hardness values around 7.5 GPa, and only the film grown at the lowest N_2 partial pressure increases to 10.5 GPa. The film-only hardness values for the sample series deposited at −40 V bias exhibits a steady increase from 14 up to 18 GPa with a decreasing N_2 fraction in the discharge gas.

The hardness over modulus ratios (H/E) for the presented films range from 0.14 up to almost 0.2, compared to values of approximately 0.07 for Si (110) and 0.072 for Al_2O_3 (0001). The H/E ratio is used to describe the deformation mechanism of the material, that is, if it is more likely to deform plastically (plastic flow, cracking) or elastically ($H/E>0.1$), for example, in a tribological asperity contact.[1]

It has to be noted that the films, especially the softer CN_x films, exhibit a tendency to creep under load, which is more pronounced for the higher stresses induced by a cube corner indenter. This creep effect can be seen for the cube corner indents in Fig. 10, where at a 10-s hold section at the maximum load, the displacement increases with time. This effect was less pronounced at lower loads, and the indents for the hardness and modulus calculation were made without a hold segment to reduce the influence of the creep.

It has been shown that for certain deposition conditions, CN_x can develop high levels of intrinsic stress.[30–35,37] For the parameters used during this study, a maximum compressive stress of −2.8 GPa was observed at a N_2 fraction of 0.16, and it stays fairly constant at this high level up to a N_2 fraction of 0.5 (Fig. 14). For N_2 fractions above 0.5, the compressive stress drops suddenly to approximately −500 MPa. For the C films grown in an Ar discharge, no intrinsic stress is observed, which is not surprising for the under-dense and voided structure. An increase in bias to −40 V at a N_2 fraction of 0.5 leads to a slightly higher value of intrinsic stress.

DISCUSSION

Effects of a coupled field on the plasma

The trapping of the plasma from a single target in a mirror magnetic field of a second target leads to more homogenous growth conditions across the sample holder, as can be seen in Fig. 2. More importantly, this also results in a reduced ion flux density of 150 μA/cm^2 (Table I) as compared to a single magnetron, while the neutral flux is kept at the same level. A decreased ion-to-neutral arrival rate ratio leads to a lower average energy per incoming particle. The resulting lower energetic growth conditions enable the evolution of the sensitive FL microstructure. For comparison, the ion flux of approximately 150 μA cm^{-2} is roughly one order of magnitude lower than in previous studies.[10] Through variation of the N_2 fraction in the Ar/N_2 discharge, a wide range of different FL structures can be fabricated with a large variation in curvature, extent, and alignment of fullerene-like CN_x sheets.

A drawback of the fairly weak plasma in the vicinity of the substrate is the low self-floating potential. This results in a small voltage drop across the sheath, giving a very low ion energy of approximately 8 eV. An external bias voltage then needs to be applied, in order to increase the voltage drop across the sheath and therefore to raise the energy of the bombarding ions to enable desired ion–surface interactions, in this case to either 25 or 40 eV.

Effects of the reduced ion flux on nitrogen incorporation

As stated in previous studies[5,20,38] the availability of nitrogen is essential for the formation of dense, solid, and textured CN_x films. Films grown without nitrogen under the stated growth conditions are completely amorphous and voided, leading to under-dense, porous material.

The ion energies of 25 or 40 eV are comparable to the energies used in Ref. 10. Thus, the observed changes in the films can be attributed to a decreased flux only. The total level of N incorporation, ranging from 13 up to 18 at. %, depends on the partial pressure and ion energy. Despite the much lower ion flux, the N incorporation is, interestingly, comparable to the previously studied films grown by reactive sputtering with a single magnetron.[10] This points to a complex film growth process as discussed below.

It is well established that the N incorporation is limited by a temperature-enhanced desorption process of volatile CN species from the growing surface.[39–43] In the present study, the N concentration remained at the same level even for a one-order-of-magnitude different ion flux density as compared to Ref. 10. This leads to the conclusion that the total

Downloaded 17 Mar 2003 to 148.6.104.15. Redistribution subject to AIP license or copyright, see http://ojps.aip.org/japo/japcr.jsp

ion flux density can have only a minor effect on the chemical desorption process. The likely explanation is that only a certain amount of nitrogen can actually be incorporated into a certain CN_x structure, and any additional N incorporation has to take place at interstitial positions, which is not possible at low energies. Hence, the structure evolution and therefore the amount of incorporated nitrogen is predominantly contingent upon the composition of the neutral flux. The growth temperature, and to a smaller extent the ion energy, also has a selective influence by providing desorption energy for volatile CN species and by enhancing surface diffusion.

Effects of N_2 partial pressure and ion energy on the film

For low-energy (25 eV) ion bombardment and a low N_2 partial pressure (which means reduced availability of N-containing species), the CN_x film consists of extensively bent and frequently intersecting planes. With a bulk N concentration of approximately 13 at. %, under these conditions, the arriving species nucleate to form features with a spherical curvature with a diameter of 0.7 nm, which are subsequently overgrown by another CN_x sheet, adding a concentric, hemispheric, dome-shaped shell around the first one at a distance of $\sim$0.35 nm. This process continues up to a diameter of approximately 5 nm, which results in 7–10 shells. The structure might be compared to a chopped onion, here referred to as a ''nano-onion.''

Fine-probe electron energy-loss spectra measurements revealed the highest nitrogen concentration in the center of the nano-onions.[8] This reinforces the notion that the incorporation of nitrogen induces curvature: (1) the p-orbital lone-pair from a sp^2 hybridized N makes for a nonplanar coordination of the three bonds; (2) nitrogen incorporation favors the formation of pentagons instead of hexagons, thus inducing curvature into a atomic sheet of carbon;[5] (3) N might also promote the adjacent C atom in a ring structure to change into a nonplanar sp^3 hybridization state.[9] Hence, the maximum feature size would be limited by the possibility to incorporate N at the growth surface under a constant supply, since fewer and fewer curved shells have to be formed to enclose the existing structure with an increasing radius. For a limited nucleation rate, assisted by the substrate temperature and ion bombardment, a competition between incorporation and desorption determines a steady-state growth of evenly sized nano-onions (see Fig. 8).

These multiwalled hemispheres having a diameter of 5 nm constitute a solid material with a strong cohesion in between the single features. This is reflected in a hardness of approximately 11 GPa and a modulus of 76 GPa. The preferred fracture path is along the outer shells of the nano-onions, as seen at the tear edge in Fig. 8. Thus, the cohesion inside the nano-onions must be even stronger. The frequently intersecting and cross-linked FL planes apparently have the ability to compress their graphitic interplanar lattice spacing by buckling during load, while slip is hindered due to cross-linkage and geometrical interlocking. This relates to the fact that most of the deformation is stored elastically and recovers after unload.

A further increase in N_2 partial pressure leads to a slightly increased nitrogen concentration in the film. Correspondingly the microstructure changes into a more pronounced graphite-like appearance, with large, meandering, and well-aligned sheets. The measured interplanar lattice spacing of approximately 0.35 nm between the sheets implies that the assembly has only weak interplanar van der Waals bonds, which limits its mechanical response as probed by nano-indentation. These films exhibit a much lower hardness and modulus, while retaining their extreme elasticity and high H/E ratio. This might again be explained by a compression of the $\sim$0.35-nm in-plane lattice spacing over large areas during loading of the material. Naturally, the van der Waals potential is much weaker and therefore the sheets are densified easily, leading to large displacements and a low modulus of approximately 40 GPa. On the other hand, the compression of the sheets is reversible, since most of the energy is stored elastically in the form of deflected atomic bonds rotated over a cone of constant angle or with slightly deflected bond-angles, enabling a high elastic recovery after unloading. This model is supported by the distribution of cross-linking sites, such that a slip of the graphitic segments is hindered.

For a slight increase in ion energy of 15 eV to approximately 40 eV, the microstructure changes independently of the nitrogen concentration in the film, which is saturated at around 18 at. % for the N_2 partial pressures used, limited by the chemical desorption process. This series of samples exhibits a pronounced FL growth at low N_2 partial pressures. An increase in N_2 partial pressure suppresses the growth of FL sheets until the material grown in a pure N_2 discharge develops an apparently amorphous structure. This results in a dramatically increased hardness and modulus to typical values of 14–18 GPa and 100–120 GPa, respectively (see Fig. 13).

In summary, it can be said that the structure and properties change dramatically with the N_2 partial pressure even though the nitrogen content in the film does not vary significantly. Interestingly, the incorporation rate, representing the number of atoms incorporated per m^2/s, increases with the availability of N_2, as seen in Table II. This is the opposite effect, as expected for a nitrogen-enhanced chemical desorption process only. We speculate that there is an increased flux from the target at higher N_2 partial pressures, which offsets the material loss by chemical desorption.[44] The effect is less distinctive in the case of a higher bias voltage. This can be explained by a higher nitrogen-stimulated chemical desorption rate at a higher bombarding energy.

It is shown in Table II that the number of incorporated particles is comparable to, and even less than, the number of ions bombarding the growing surface, indicating the importance and extent of the material removal by the chemical desorption process. Keeping in mind that the flux for a sputtering discharge consists predominantly of neutrals, only a very limited fraction of the total flux is actually incorporated. It can also be useful to consider the film structures grown as those representing a dynamic equilibrium between the competing processes of deposition fluxes of given species and film surface etching rates, both determined by the N_2 frac-

Downloaded 17 Mar 2003 to 148.6.104.15. Redistribution subject to AIP license or copyright, see http://ojps.aip.org/japo/japcr.jsp

tion, growth temperature, and bias voltage. The features of the prevailing structures in the CN_x compounds need not to be linked to the N concentration in the film. This can be illustrated by a comparison of the two sample series. The films grown at a higher bias voltage have a lower incorporation rate, but slightly higher nitrogen content. This can be explained by a different etching/desorption rate at the higher-energy regime.[45] It might be more favorable, under these conditions, to remove volatile particles with a higher C content from the surface, giving more reactive sites for nitrogen or preformed nitrogen-containing species to bond to. The resulting structure in that case is characterized by a reduced long-range order of the fullerene-like sheets, leading to an amorphous appearance. The reduced extent of these FL sheets gives rise to a higher degree of cross-linkage along the edges, which results in the astonishingly fracture-tough compounds.

Intrinsic stress formation in fullerene-like CN_x

The homogeneity of the film growth across the 75-mm sample holder made it possible to derive the intrinsic stress *in situ*, by monitoring the curvature of a Si wafer. The compressive stress reaches peak values of up to -2.7 GPa for films grown at a low N_2 fraction. These are surprisingly high values, since neither the energy nor the number of ions is large enough to explain the stress formation by conventional models for intrinsic stress generation. The formation of intrinsic stresses in CN_x cannot be related to conventional momentum transfer and collision cascade models, since the ion energies involved are too low for, for example, atomic peening.[34] The presented results indicate that the high levels of stress are closely linked with the formation of the FL structure, and the stress scales with the degree of curvature of the graphitic planes. This curvature has to be accommodated in an already existing structure in which the graphitic sheets are restricted in lateral motion, which leads to the formation of high levels of compressive stress.[35] This notion is reinforced by the fact that the stress level does not exceed -500 MPa for films consisting of less bent planes, in the case of pure N_2 and 25 eV energy. The stress state is still in compression, which is not surprising, since a certain amount of curvature has to be accommodated.

CONCLUSIONS

The reduction of the ion flux in the vicinity of the substrate by a magnetic field from a second magnetron enables the formation of a more pronounced fullerene-like microstructure in CN_x films as compared to previous techniques employing reactive magnetron sputtering or pulsed laser deposition. This covers a broad range of different radii of curvature and regimes of sheet alignment and extension. The microstructure of FL CN_x is found to be extremely sensitive to the deposition conditions. It is shown that the resulting FL structures have, in turn, characteristic mechanical properties. An increase in curvature of the FL lattice planes leads to a reduced long-range order. Therefore, the planes are more frequently intersecting and/or cross-linking, giving the structure more strength, as seen for films grown at 40-eV ion energy and lower N_2 fractions with elastic moduli of approximately 120 GPa. If the structure is instead composed of extended well-aligned planes, the modulus is reduced by up to a factor of 3, due to a less restricted compression of the interplanar lattice spacing and a lack of cross-linkage. This makes for a low elastic modulus and large maximum displacements.

FL CN_x materials are best described by a high hardness-to-modulus ratio (H/E) of up to 0.2, which explains the extreme elasticity of this material even for a fairly low intrinsic hardness of the samples produced. In the absence of plastic deformation the contact stresses are dissipated over larger volumes. Therefore, it follows that FL CN_x can be perceived as a "super-hard rubber,"[1] rather than a conventional hard material.

The synthesis of FL CN_x is a rather complex process, in which the microstructure cannot be exclusively linked to the N content in the film alone. One also has to pay close attention to the number and kinds of species arriving/desorbing from the substrate, in addition to the substrate temperature and energy of the ionized species. The corresponding equilibrium defines the resulting structure.

ACKNOWLEDGMENTS

This work was supported by SKF/ERC, the EC-TMR program, the Swedish Foundation for Strategic Research (SSF) "Materials Research Program for Low-Temperature Thin Film Synthesis." The ERDA measurements were carried out at the Research Center Rossendorf (Germany), Institute of Ion Beam Physics and Materials Research with the support from Dr. U. Kreissig, financed by the European Community "Access to Research Infrastructure–action of the Improving Human Potential" program. The authors would like to thank S. J. Bull and I. Arce Garcia from Newcastle University for valuable discussions on the nanoindentation evaluation. Valuable discussions with N. Hellgren are also greatly acknowledged.

[1] I. Arce Garcia, E. R. Berasategui, S. J. Bull, T. F. Page, N. Hellgren, J. Neidhardt, and L. Hultman, Philos. Mag. A **82**, 2133 (2002).
[2] E. Broitman, N. Hellgren, O. Wänstrand, M. P. Johansson, T. Berlind, H. Sjöström, J.-E. Sundgren, M. Larsson, and L. Hultman, Wear **248**, 55 (2001).
[3] L. Hultman, S. Stafström, Z. Czigány, J. Neidhardt, N. Hellgren, I. F. Brunell, K. Suenaga, and C. Colliex, Phys. Rev. Lett. **87**, 225503 (2001).
[4] A. A. Voevodin, J. G. Jones, Zs. Czigány, L. Hultman, and J. S. Zabinski, J. Appl. Phys. (in press).
[5] H. Sjöström, S. Stafström, M. Boman, and J.-E. Sundgren, Phys. Rev. Lett. **75**, 1336 (1999).
[6] I. Petrov, A. Myers, J. E. Greene, and J. R. Abelson, J. Vac. Sci. Technol. A **12**, 2846 (1994).
[7] C. M. Brown, E. Beer, C. Bellavia, L. Cristofolini, R. González, M. Hanfland, D. Häusermann, M. Keshavarz-K, K. Kordatos, K. Prassides, and F. Wudl, J. Am. Chem. Soc. **118**, 8715 (1996).
[8] Zs. Czigány, I. F. Brunell, J. Neidhardt, K. Suenaga, and L. Hultman, Appl. Phys. Lett. **79**, 2639 (2001).
[9] S. Stafström, Appl. Phys. Lett. **77**, 3941 (2000).
[10] N. Hellgren, K. Macák, E. Broitman, M. P. Johansson, L. Hultman, and J.-E. Sundgren, J. Appl. Phys. **88**, 524 (2000).
[11] E. Chason, J. A. Floro, *Materials Reliability in Microelectronics VI Symposium* 1996, p. 499.
[12] D. N. Ruzic, *Electric Probes for Low Temperature Plasma*, edited by W. Weed, American Vacuum Society Monograph Series (AVS Education Committee, New York, 1994).

Downloaded 17 Mar 2003 to 148.6.104.15. Redistribution subject to AIP license or copyright, see http://ojps.aip.org/japo/japcr.jsp

[13] J. R. Tesmer, M. Nastasi, *Handbook of Modern Ion Beam Materials Analysis* (Materials Research Society, Pittsburgh, 1995).
[14] C. L. Woodcock and D. F. Bahr, Scr. Mater. **43**, 783 (2000).
[15] E. Martínez and J. Esteve, Appl. Phys. A: Mater. Sci. Process. **72**, 319 (2001).
[16] W. C. Oliver and G. M. Pharr, J. Mater. Res. **7**, 1564 (1992).
[17] C. Fischer-Cripps, J. Mater. Sci. **34**, 129 (1999).
[18] M. Korunsky, M. R. McGurk, S. J. Bull, and T. F. Page, Surf. Coat. Technol. **99**, 171 (1998).
[19] Zs. Czigány, J. Neidhardt, I. F. Brunell, and L. Hultman, Ultramicroscopy (in press).
[20] N. Hellgren, M. P. Johansson, E. Broitman, L. Hultman, and J.-E. Sundgren, Phys. Rev. B **59**, 5162 (1999).
[21] C. Ronning, H. Feldermann, R. Merk, H. Hofsäss, P. Reinke, and J.-U. Thiele, Phys. Rev. B **58**, 2207 (1998).
[22] S. Souto, M. Pickholz, M. C. dos Santos, and F. Alvarez, Phys. Rev. B **57**, 2536 (1998).
[23] N. Hellgren, J. Guo, C. Såthe, A. Agui, J. Nordgren, Y. Luo, H. Ågren, and J.-E. Sundgren, Appl. Phys. Lett. **79**, 4348 (2001).
[24] W. T. Zheng, K. Z. Xing, N. Hellgren, M. Lögdlund, Å. Johansson, U. Gelius, W. R. Salaneck, and J.-E. Sundgren, J. Electron Spectrosc. Relat. Phenom. **87**, 45 (1997).
[25] M. A. Baker and P. Hammer, Surf. Interface Anal. **25**, 629 (1997).
[26] W. F. Egelhoff, Jr., Surf. Sci. Rep. **6**, 253 (1986).
[27] D. Briggs and M. P. Seah, *Auger and X-ray Phototelectron Spectroscopy*, in Practical Surface Analysis Vol. 1 (Wiley, Chichester, England, 1990).
[28] T. F. Page and S. Hainsworth, Surf. Coat. Technol. **61**, 201 (1993).
[29] Th. Malkow, I. Arce Garcia, A. Kolitsch, D. Schneider, S. J. Bull, and T. F. Page, Diamond Relat. Mater. **10**, 2199 (2001).
[30] V. S. Veerasamy, J. Yuan, G. A. J. Amaratunga, W. I. Milne, K. W. R. Gilkes, M. Weiler, and L. M. Brown, Phys. Rev. B **48**, 17954 (1993).
[31] C. A. Davis, D. R. McKenzie, Y. Yin, E. Kravtchinskia, G. A. J. Amaratunga, and V. S. Veerasamy, Philos. Mag. B **69**, 1133 (1994).
[32] M. Chhowalla, I. Alexandrou, C. Kiely, G. A. J. Amaratunga, R. Aharonov, and R. Fonatana, Thin Solid Films **290/291**, 103 (1996).
[33] R. Kaltofen, T. Sebald, and G. Weise, Thin Solid Films **290/291**, 112 (1996).
[34] J. Bulir, M. Jelinek, V. Vorlicek, J. Zemek, and V. Perina, Thin Solid Films **292**, 318 (1997).
[35] E. Broitman, W. T. Zheng, H. Sjöström, I. Ivanov, J. E. Greene, and J.-E. Sundgren, Appl. Phys. Lett. **72**, 2532 (1998).
[36] C. A. Davis, Thin Solid Films **226**, 30 (1993).
[37] I. F. Brunell, L. Picon, Z. Czigány, J. Neidhardt, N. Hellgren, and L. Hultman (unpublished).
[38] H. Sjöström, I. Ivanov, M. Johansson, L. Hultman, L. R. Wallenberg, J.-E. Sundgren, S. V. Hainsworth, and T. F. Page, Thin Solid Films **246**, 103 (1994).
[39] S. S. Todorov, D. Marton, K. J. Boyd, A. H. Al-Bayati, and W. J. Rabalais, J. Vac. Sci. Technol. A **12**, 3192 (1994).
[40] P. Hammer and W. Gissel, Diamond Relat. Mater. **5**, 1152 (1996).
[41] R. Kaltofen, T. Sebald, and G. Weise, Thin Solid Films **308/309**, 118 (1997).
[42] C. Spaeth, U. Kreissig, and F. Richter, Thin Solid Films **355/356**, 64 (1999).
[43] N. Hellgren, M. P. Johansson, E. Broitman, P. Sandström, L. Hultman, and J.-E. Sundgren, Thin Solid Films **382**, 146 (2001).
[44] J. Neidhardt, B. Fritsche, R. Gago, W. Möller, and L. Hultman (unpublished).
[45] N. A. Morrison, S. E. Rodil, J. Robertson, and W. I. Milne, J. Appl. Phys. **89**, 5754 (2001).

Downloaded 17 Mar 2003 to 148.6.104.15. Redistribution subject to AIP license or copyright, see http://ojps.aip.org/japo/japcr.jsp